

Article

Effect of Small Molecular Organic Acids on the Structure and Catalytic Performance of Sol–Gel Prepared Cobalt Cerium Oxides towards Toluene Combustion

Jianmeng Chen ^{1,2}, Junhong Lin ¹, Jinghuan Chen ^{1,*}  and Jiade Wang ^{1,2}

¹ College of Environment, Zhejiang University of Technology, Hangzhou 310014, China; jchen@zjut.edu.cn (J.C.); linjh89@163.com (J.L.); jdwang@zjut.edu.cn (J.W.)

² Key Laboratory of Microbial Technology for Industrial Pollution Control of Zhejiang Province, Zhejiang 310000, China

* Correspondence: chenjh@zjut.edu.cn

Received: 9 May 2019; Accepted: 23 May 2019; Published: 24 May 2019



Abstract: Cobalt cerium oxide catalysts with small molecular organic acids (SOAs) as chelating agents were prepared via the sol–gel method and investigated for the complete oxidation of toluene. Four kinds of natural SOAs, i.e. malic acid (MA), citric acid (CA), glycolic acid (GA), and tartaric acid (TA), were selected. The effect of organic acids on the composition, structure, morphology and catalytic performance of metal oxides is discussed in details. The cobalt cerium oxides catalysts were characterized by various techniques, including TG–DSC, XRD, SEM–EDS, N₂–adsorption and desorption, XPS, and H₂–TPR analyses. The results show that the nature of organic acids influenced the hydrolysis, condensation and calcination processes, as well as strongly affected the textural and physicochemical properties of the metal oxides synthesized. The best catalytic activity was obtained with the CoCe–MA catalyst, and the toluene conversion reached 90% at 242 °C. This outstanding catalytic activity could be related to its textural, redox properties and unique surface compositions and oxidation states. In addition, the CoCe–MA catalyst also showed excellent stability in long–time activity test.

Keywords: Cobalt cerium oxides; ceria; sol–gel method; catalytic oxidation; volatile organic compounds; toluene; oxygen species

1. Introduction

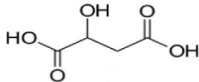
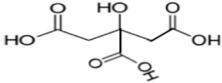
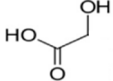
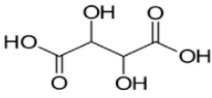
Volatile organic compounds (VOCs), as the main precursors of ozone and smog [1], not only do harm to the environment, but also endanger human health [2–4]. Therefore, control of VOCs emission has become an urgent environmental issue. Catalytic oxidation, one of the most effective control technologies for VOCs, has been widely studied in the past decade [5,6]. The performance of the oxidation catalyst is regarded as a key factor in determining the efficiency of catalytic oxidation technique [7,8]. VOCs total oxidation catalysts mainly include transition metal oxides and noble metals [9]. Noble metal catalysts have the advantages of high catalytic activity and low ignition temperature [10,11]; nevertheless, the high cost limits their wide application. Therefore, in recent years, transition metal oxide catalysts [12,13], such as Mn, Cu, Cr, Fe, and Co oxides, are becoming increasingly popular [14,15]. Among these catalysts, Co₃O₄ is one of the most powerful oxides for VOCs oxidation [16]. Besides, CeO₂, a typical rare earth oxide, has excellent redox property and oxygen transfer ability [17], thus, it is widely used as a catalyst promoter in VOCs oxidation reaction [18]. Liotta et al. [19] and Michalis et al. [20] investigated the catalytic performance of Co₃O₄–CeO₂ binary

oxides and found that CeO₂ promoted the reducibility of Co₃O₄ and the synergistic interaction between cobalt and cerium species. Therefore, cobalt cerium oxides catalysts were selected in this study to evaluate their performance in VOC oxidation.

Various methods, including sol–gel technique [21], co–precipitation method [22], and hydrothermal process [23], have been developed to synthesize metal oxides catalysts. Among them, the sol–gel method has been extensively studied in the synthesis of mixed metal oxides for the complete oxidation of VOCs, such as Co–Ce [21], Ce–Ti [24], Cu–V [25], Cu–Ce [26], and Ce–Fe [27] mixed metal oxides. As revealed in [28], the sol–gel process consists of hydrolysis and condensation reactions of metal precursors. The hydrolysis allows the formation of hydroxyl groups (M–OH, M: represents metal) that subsequently condense into strong and rigid metal–oxo–metal bridges (M–O–M) [29]. In the sol–gel process, the chelating agent plays an important role in the above two chemical reactions because it changes the gel structure by affecting the reaction rate of hydrolysis and condensation. In recent years, some researchers tried to use carboxylic acids as chelating agents in the sol–gel process and investigated their roles in phase formation and magnetic or electrochemical properties of the materials synthesized [30,31]. However, the effects of type of organic acids on the composition, structure, morphology and catalytic performances of metal oxides have not been mentioned before. On the other hand, the citric acid method, as one kind of sol–gel methods, has been widely utilized in the preparation of metal oxides. However, as there are many small–molecule organic acids sharing similar characteristics with citric acid, can we substitute citric acid with other organic acids in the preparation process to develop catalysts with superior performance? Therefore, it is necessary to investigate the influence of SOAs on the structure and catalytic properties of metal oxide catalysts and then develop high–efficient catalysts for VOCs abatement.

In this study, with the aim of developing effective catalysts, four kinds of natural SOAs, i.e. malic acid (MA), citric acid (CA), glycolic acid (GA), and tartaric acid (TA), were chosen as chelating agents for the sol–gel synthesis of cobalt cerium oxides. Their chemical formula, molecular structure and part of the physical properties are summarized in Table 1. The chosen organic acids have different numbers of hydroxyl groups as well as carboxyl groups. Thus, they can serve as chelating media and are commonly used in the sol–gel method. In this work, Cobalt cerium oxide catalysts were synthesized with four kinds of organic acids as chelating agents. The effect of different organic acids on the physicochemical properties of the catalysts was confirmed by thermogravimetric analysis–differential scanning calorimetry (TG–DSC), X–ray diffractometer (XRD), scanning electron microscopy–energy dispersive spectroscopy (SEM–EDS), N₂–adsorption and desorption, X–ray photoelectron spectroscopy (XPS) and hydrogen temperature programmed reduction (H₂–TPR). The structure–activity relationship between cobalt cerium oxide catalysts and toluene conversion rate was investigated.

Table 1. The molecular structure and part of the physical properties of the organic acids selected.

Organic Acid	Abbreviation	Chemical Formula	Structure	Molecular Mass (g/mol)	Boiling Points (°C)	$\Delta_c H_m^\theta$ (kJ/mol) ^a
Malic acid	MA	C ₄ H ₆ O ₅		134.1	140	-1326.5
Citric acid	CA	C ₆ H ₈ O ₇		192.1	175	-1952.8
Glycolic acid	GA	C ₂ H ₄ O ₃		76.1	100	-695.3
Tartaric acid	TA	C ₄ H ₆ O ₆		150.1	170	-1141.1

^a The standard molar heat of combustion ($\Delta_c H_m^\theta$) data were obtained from the manual of physical chemistry.

2. Results

2.1. TG–DSC Results

The TG–DSC results of the uncalcined CoCe–X samples are shown in Figure 1. As can be seen in the figure, two weight–loss steps were observed. The first weight–loss step occurred below approximately 350 °C and can be attributed to the combustion of residual organic acids and the pyrolysis of NO_3^- and organic phases to give an amorphous inorganic phase [5,32]. The second weight–loss step was due to the further transformation of amorphous inorganic phase into crystalline inorganic phase [33]. Additionally, in the DSC curves, the first weight–loss step was accompanied by a strong exothermic peak, which was centered at 262, 327, 277 and 297 °C, respectively. It was interesting to find that the sequences of the heat released as well as the weight–loss percentage in the first step of the four samples were consistent with that of the standard molar burning enthalpy of the organic acids used. In other words, the higher was the standard molar burning enthalpy of the organic acid (Table 1), the more heat was released and the more weight was lost. This result suggest that the thermal properties of SOAs had an important role in the formation of metal oxides prepared by the sol–gel method.

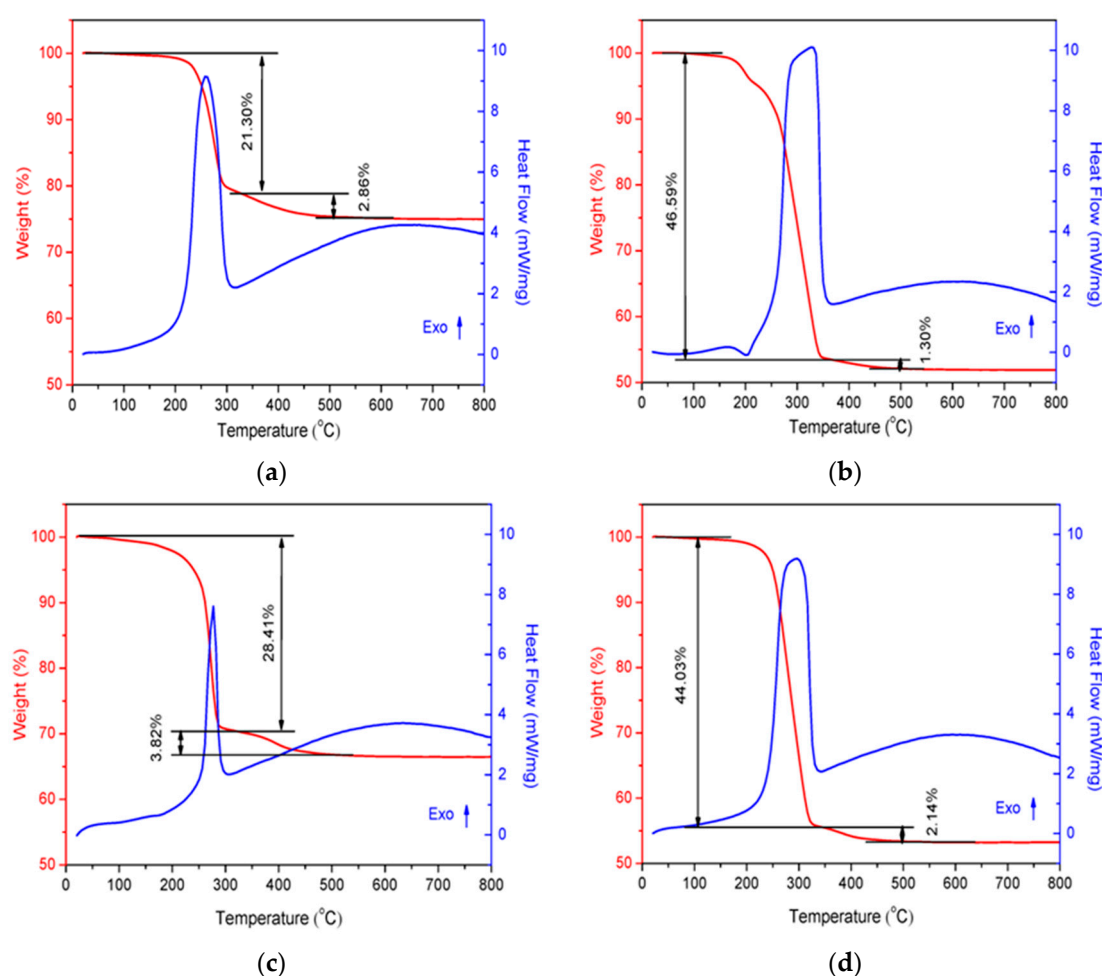


Figure 1. TG–DSC curves of the CoCe–X precursors: (a) CoCe–MA; (b) CoCe–CA; (c) CoCe–GA; and (d) CoCe–TA.

2.2. XRD Results

The XRD patterns of all synthesized catalysts are presented in Figure 2. The diffraction peaks at 19.0°, 31.3°, 36.8°, 38.5°, 44.8°, 59.4°, and 65.4° were ascribed to spinel phase Co_3O_4 (JCPDS 74–1656), and the other diffraction peaks at 28.5°, 33.1°, 47.5°, and 56.3° could be assigned to fluorite phase CeO_2

(JCPDS 43–1002). It was observed that the intensity and width of the characteristic diffraction peaks of the CoCe–X catalysts varied with different organic acids used. The peak intensity of the CoCe–GA and CoCe–TA catalysts were stronger than those of the CoCe–MA and CoCe–CA catalysts.

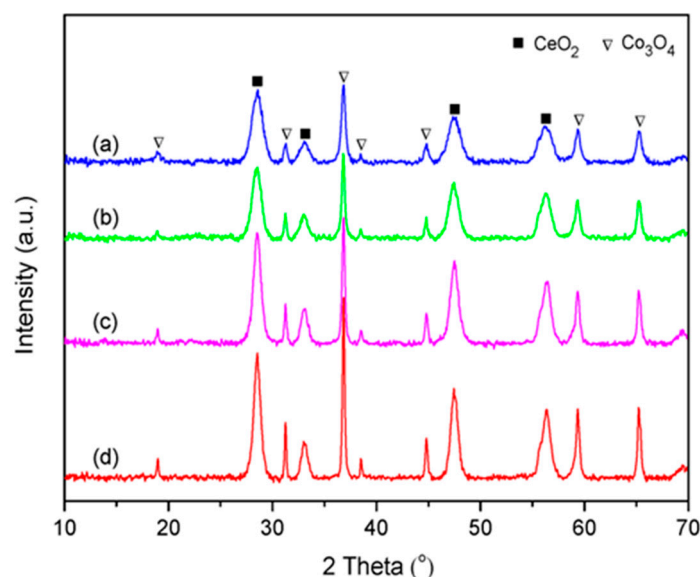


Figure 2. XRD patterns of the CoCe–X catalysts: (a) CoCe–MA; (b) CoCe–CA; (c) CoCe–GA; and (d) CoCe–TA.

The crystallite sizes of CeO₂ and Co₃O₄ of the CoCe–X catalysts were calculated by the Scherrer equation, as listed in Table 2. The crystallite sizes of CeO₂ and Co₃O₄ shared the same sequence, which was as follows: CoCe–MA < CoCe–CA < CoCe–GA < CoCe–TA. In addition, the crystallite sizes of CeO₂ were much smaller than those of Co₃O₄. These differences may be related to the acidity and molecular structure of organic acids used because the acidity could affect the speed of metal hydrolysis, while the molecular structure may influence the dispersion of the colloidal particles in the solution, as reported in the literature [31,34].

Table 2. Crystallite sizes and structural parameters of the CoCe–X catalysts.

Sample	Crystallite Size of CeO ₂ (nm) ^a	Crystallite Size of Co ₃ O ₄ (nm) ^b	BET Surface Area (m ² /g)	Average Pore Volume (cm ³ /g)	Average Pore Diameter (nm)
CoCe–MA	9.6	19.8	40.3	0.153	11.7
CoCe–CA	10.0	25.8	21.1	0.071	10.8
CoCe–GA	11.5	30.2	14.5	0.069	12.3
CoCe–TA	12.8	38.2	14.3	0.041	9.2

^{a,b} The crystallite sizes of CeO₂ and Co₃O₄ (diffraction peak at 28.5° and 36.8°, respectively) were estimated by the Scherrer equation.

2.3. N₂–Adsorption and Desorption Results

To obtain structural parameters of the CoCe–X catalysts, N₂–adsorption and desorption of the CoCe–X catalysts were carried out. The N₂–adsorption and desorption isotherms of the CoCe–X catalysts are depicted in Figure 3. As shown in Figure 3, the CoCe–X catalysts displayed typical IV isotherms with H₁–type hysteresis loops, which indicated the existence of mesopores [35]. The BET surface areas (*S*_{BET}), average pore volumes (*V*_p), and average pore sizes (*D*_p) are summarized in Table 2. In Table 2, the *S*_{BET} and *V*_p of the CoCe–MA catalyst were 40.3 m²/g and 0.153 cm³/g, respectively, which were larger than those of the other catalysts.

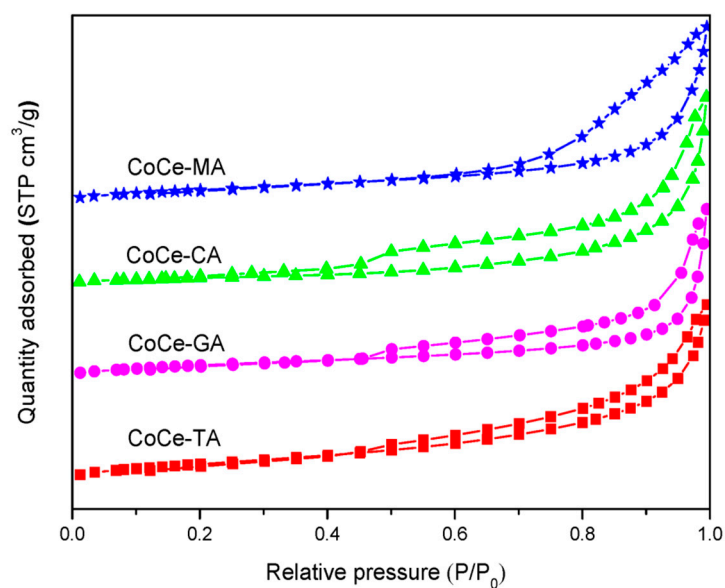


Figure 3. N_2 adsorption and desorption isotherms of the CoCe-X catalysts.

2.4. SEM-EDS Results

The SEM images of the CoCe-X catalysts are shown in Figure 4. As can be seen in the figure, the CoCe-X samples exhibited a porous structure, and the pore size of the CoCe-MA catalyst was relatively larger than those of the other catalysts. In addition, agglomeration of small particles was observed on the surface of CoCe-GA and CoCe-TA catalysts. As revealed by TG-DSC, during the calcination process below 350 °C, there was a distinct exothermic process, which released a large volume of gases and the gel swelled into porous materials. Thus, the textural properties of cobalt cerium oxides catalysts greatly depended on the type of the chelating agent used.

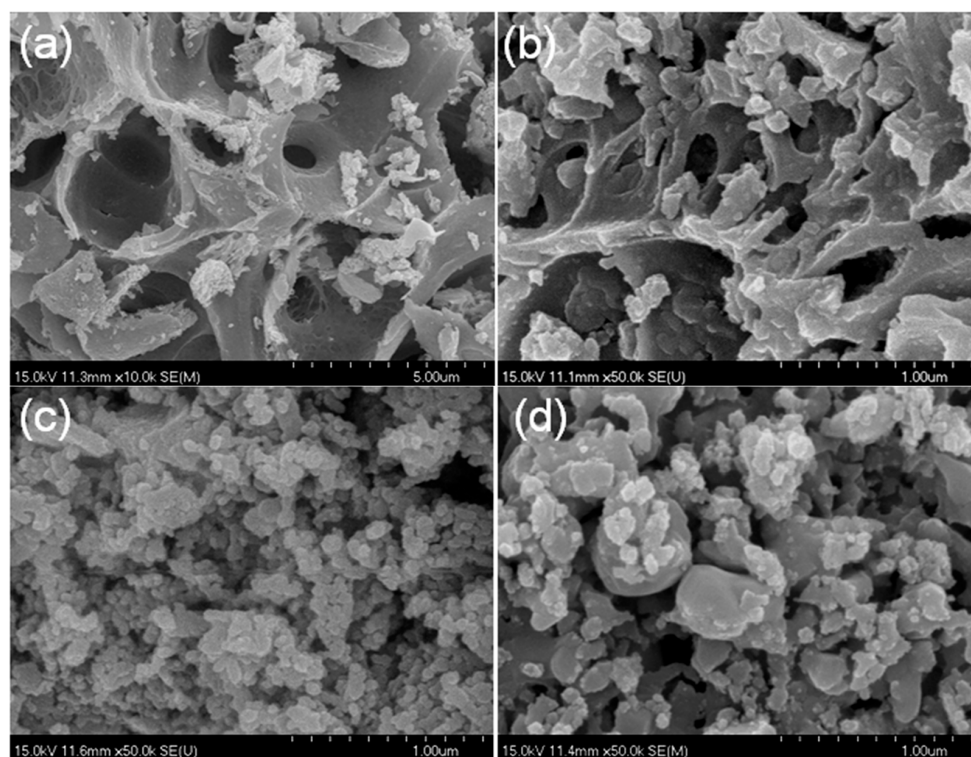


Figure 4. SEM images of the CoCe-X catalysts: (a) CoCe-MA; (b) CoCe-CA; (c) CoCe-GA; and (d) CoCe-TA.

Elemental content of the CoCe–X catalysts is summarized in Table 3. The CoCe–X catalysts were mainly composed of cobalt, oxygen, and cerium. In all samples, the mass percentage of cobalt, oxygen, and cerium was similar.

Table 3. Elemental content of the CoCe–X catalysts.

Sample	Elemental Content (wt.%) ^a		
	O	Co	Ce
CoCe–MA	10.76	39.95	49.29
CoCe–CA	10.65	40.21	49.14
CoCe–GA	10.92	39.82	49.26
CoCe–TA	11.05	41.06	47.89

2.5. XPS Results

To obtain detailed information of the surface composition and local atomic environments of the CoCe–X catalysts, XPS measurements were carried out. The O 1s, Co 2p, and Ce 3d XPS spectra of the CoCe–X catalysts are shown in Figure 5A–C. The XPS results of the CoCe–X catalysts are summarized in Table 4.

Table 4. XPS results of the CoCe–X catalysts.

Sample	Binding Energy (eV)						Atomic Ratio		
	O 1s		Co 2p _{3/2}		Ce 3d _{5/2}		O _{ads} /O _{lat}	Co ²⁺ /Co ³⁺	Ce ³⁺ /Ce ⁴⁺
	O _{lat}	O _{ads}	Co ²⁺	Co ³⁺	Ce ³⁺	Ce ⁴⁺			
CoCe–MA	529.9	531.4	782.2	779.8	885.8	882.6	0.40	0.35	0.22
CoCe–CA	529.9	531.4	782.9	779.9	885.7	882.4	0.36	0.33	0.20
CoCe–GA	529.9	531.5	782.5	779.9	886.0	882.5	0.35	0.30	0.19
CoCe–TA	529.9	531.4	782.7	779.9	885.6	882.6	0.33	0.28	0.17

As shown in Figure 5A, the XPS spectra of O 1s was decomposed into two bands. The first one located at 529.9 eV, which could be attributed to the lattice oxygen, O_{lat} [36]. The second one at 531.4 eV was assigned to the adsorbed oxygen, O_{ads}, which was related to the oxygen species on surface oxygen vacancies [20,37]. The content of adsorbed oxygen could be estimated on the basis of the peak area ratio of O_{ads}/O_{lat}. The O_{ads}/O_{lat} values and the binding energies of O 1s are summarized in Table 4. The O_{ads}/O_{lat} value of the CoCe–MA catalyst was the highest, while the other catalysts were of the following order: CoCe–CA > CoCe–GA > CoCe–TA.

The Co 2p spectra of the CoCe–X catalysts are shown in Figure 5B. The Co 2p spectra were decomposed into two spin–orbit doublets D₁ and D₂ and two satellite peaks S₁ and S₂. The Co 2p_{3/2} peak at 779.8 eV and the Co 2p_{1/2} peak at 795.8 eV were marked as D₁, which was attributed to the Co³⁺ species. The D₂ with a binding energy of 2p level of 782.6 eV and a 2p_{3/2}–2p_{1/2} splitting of 14.6 eV corresponded to Co²⁺ species [20,37]. The surface Co²⁺/Co³⁺ atomic ratios and the binding energies of Co 2p_{3/2} are summarized in Table 4. In Table 4, the Co²⁺/Co³⁺ atomic ratios on the surface of the CoCe–X catalysts followed a sequence of: CoCe–MA > CoCe–CA > CoCe–GA > CoCe–TA. This sequence was consistent with the order of the surface O_{ads}/O_{lat} ratios. According to the literature [38,39], the amount of oxygen species adsorbed on the surface was closely related to the higher concentration of Co²⁺. Therefore, the high Co²⁺/Co³⁺ atomic ratio could indicate an increase of the surface oxygen vacancies, which may enhance the catalytic oxidation activity of the catalyst.

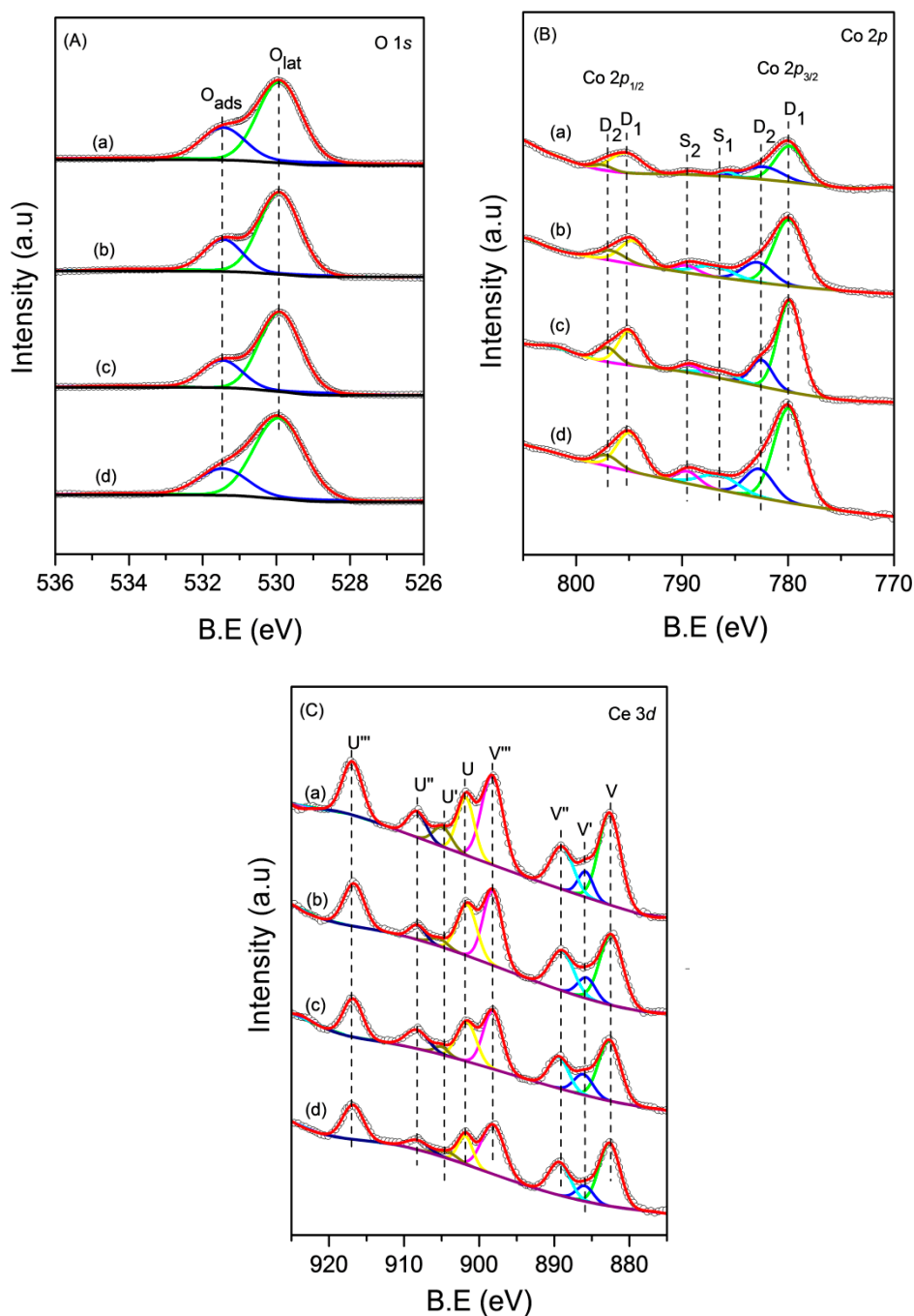


Figure 5. Experimental and fitted: (A) O 1s; (B) Co 2p; and (C) Ce 3d photoelectron spectra of the CoCe-X catalysts: (a) CoCe-MA; (b) CoCe-CA; (c) CoCe-GA; and (d) CoCe-TA.

The XPS spectra of Ce 3d are shown in Figure 5C. The peaks labeled U and V were attributed to $3d_{3/2}$ and $3d_{5/2}$ spin-orbit components, respectively [21]. In addition, the peaks at 882.4 (V), 889.0 (V''), 898.1 (V'''), 901.6 (U), 908.2 (U''), and 916.7 (U''') eV were ascribed to Ce^{4+} , whereas those at 885.8 (V') and 904.6 (U') eV were assigned to Ce^{3+} [20]. The surface Ce^{3+}/Ce^{4+} atomic ratios could be obtained by the XPS peak areas ratios of Ce $3d_{3/2}$ and Ce $3d_{5/2}$ components combined with Ce^{4+} and Ce^{3+} . The Ce^{3+}/Ce^{4+} atomic ratios and the binding energies of Ce $3d_{5/2}$ are summarized in Table 4. The surface atomic ratios of Ce^{3+}/Ce^{4+} were 0.22, 0.20, 0.19, and 0.17 for the CoCe-MA, CoCe-CA, CoCe-GA, and CoCe-TA catalysts, respectively. In other words, the CoCe-MA catalyst exhibited the highest concentration of surface Ce^{3+} species. The presence of Ce^{3+} could cause charge imbalance

and oxygen vacancies of catalysts, resulting in more active surface oxygen species [40,41]. Thus, the concentration of surface Ce^{3+} species may be closely related to the catalytic activity of the catalysts.

2.6. H_2 -TPR Results

To investigate the reduction properties of the CoCe-X catalysts, the TPR experiments were carried out. The H_2 -TPR profiles of the CoCe-X catalysts are plotted in Figure 6. Additionally, the H_2 consumption of the CoCe-X catalysts is summarized in Table 5.

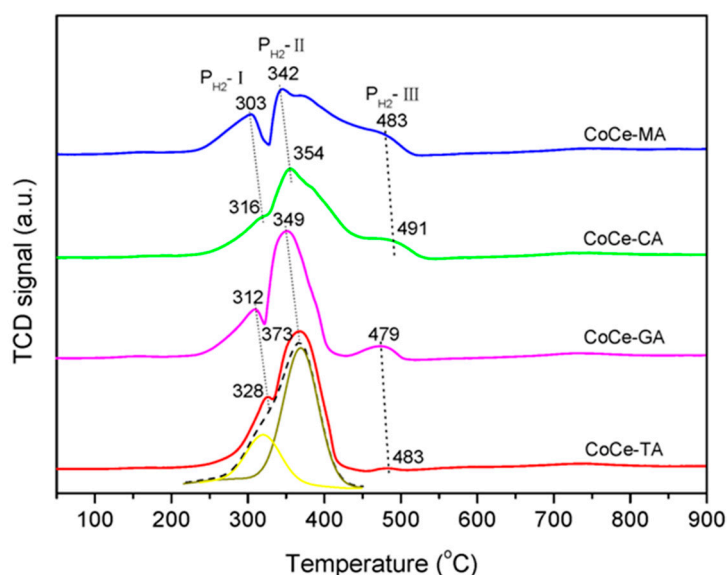


Figure 6. H_2 -TPR profiles of the CoCe-X catalysts.

Table 5. H_2 consumption and catalytic activities of the CoCe-X catalysts.

Sample	H_2 Consumption (mmol/g _{cat})				Catalytic Activity		
	$P_{\text{H}_2\text{-I}}$	$P_{\text{H}_2\text{-II}}$	$P_{\text{H}_2\text{-III}}$	Total	Ratio of $P_{\text{H}_2\text{-II}}/P_{\text{H}_2\text{-I}}$	T_{50} (°C)	T_{90} (°C)
CoCe-MA	1.84	5.33	1.41	8.58	2.90	232	242
CoCe-CA	1.91	5.71	1.10	8.72	2.99	237	245
CoCe-GA	1.89	5.80	0.60	8.29	3.07	240	250
CoCe-TA	2.19	6.55	0.05	8.74	2.99	245	256

As shown in Figure 6, three reduction peaks were observed in the temperature range of 50–900 °C. According to the literature [39,41], the first reduction peak ($P_{\text{H}_2\text{-I}}$) was attributed to the reduction of Co_3O_4 to CoO , while the second peak ($P_{\text{H}_2\text{-II}}$) was due to the further reduction of CoO to metallic cobalt [42]. In addition, the weak reduction peaks around 480 °C ($P_{\text{H}_2\text{-III}}$) could be ascribed to the reduction of surface oxygen species of CeO_2 [43,44]. As listed in Table 5, the peak area ratios of $P_{\text{H}_2\text{-II}}/P_{\text{H}_2\text{-I}}$ were in the range of 2.90–3.07, which was close to the theoretical values (the theoretical H_2 consumption ratio of $P_{\text{H}_2\text{-II}}/P_{\text{H}_2\text{-I}}$ should be 3:1). This result further confirmed that the attribution of the $P_{\text{H}_2\text{-I}}$ and $P_{\text{H}_2\text{-II}}$ should be the stepwise reduction of Co_3O_4 .

As shown in Figure 6, the peak positions of $P_{\text{H}_2\text{-I}}$ and $P_{\text{H}_2\text{-II}}$ changed with different organic acids used. For CoCe-TA, the peak temperatures of $P_{\text{H}_2\text{-I}}$ and $P_{\text{H}_2\text{-II}}$ were 328 and 373 °C, respectively, which were the highest among these catalysts. For CoCe-MA, the peak temperatures of $P_{\text{H}_2\text{-I}}$ and $P_{\text{H}_2\text{-II}}$ lowered to 303 and 342 °C, respectively. The peak temperatures for CoCe-CA and CoCe-GA were between those of CoCe-MA and CoCe-TA. Therefore, the CoCe-MA catalyst exhibited the best redox properties. These results also indicate that the type of organic acids used could strongly affect the reducibility of the samples synthesized.

It should be noted that isolated peaks attributed to the reduction of CeO_2 ($\text{P}_{\text{H}_2\text{-III}}$) could be observed in the TPR profiles of CoCe-GA and CoCe-TA, while such peaks changed in positions and were overlapped with $\text{P}_{\text{H}_2\text{-II}}$ in the TPR profiles of CoCe-MA and CoCe-CA. Additionally, compared with the TPR profiles of CoCe-GA and CoCe-TA, the peak $\text{P}_{\text{H}_2\text{-II}}$ of CoCe-MA and CoCe-CA broadened, especially for CoCe-MA. The broadening of $\text{P}_{\text{H}_2\text{-II}}$ might suggest that the reduction of Co^{2+} interacting with CeO_2 was perhaps delayed by the stabilization effect of ceria to cobalt ions at medium valence, as reported by Luo et al. [34]. Furthermore, as for $\text{P}_{\text{H}_2\text{-III}}$, the H_2 consumption of CoCe-MA and CoCe-CA were much larger than those of CoCe-GA and CoCe-TA. This result could be due to the spill-over effect of hydrogen from the Co to CeO_2 [45]. Therefore, it can be confirmed that, in the CoCe-MA and CoCe-CA catalysts, the cobalt species shared a homogeneous interaction with CeO_2 phase.

2.7. Catalytic Performance

The catalytic activity of the CoCe-X catalysts for the complete oxidation of toluene is shown in Figure 7A. As shown in Figure 7A, the CoCe-X catalysts showed good activity for toluene oxidation and the conversion rate of toluene was close to 100% at about 275 °C. T_{50} and T_{90} , i.e. the temperature required for 50% and 90% conversion, respectively, are shown in Table 5. The results show that the T_{50} and T_{90} of the CoCe-MA catalyst ($T_{50} = 232$ °C, $T_{90} = 242$ °C) were the lowest, while those of CoCe-TA catalyst ($T_{50} = 245$ °C, $T_{90} = 256$ °C) were the opposite. The T_{50} and T_{90} were 237 and 245 °C over the CoCe-CA catalyst, and 240 and 250 °C over the CoCe-GA catalyst, respectively. Therefore, when T_{90} was used as the active standard, the order of activity of the CoCe-X catalysts was as follows: CoCe-MA > CoCe-CA > CoCe-GA > CoCe-TA. For better comparison, Figure 7B demonstrates the toluene consumption rates over CoCe-X catalysts. This results further confirm the superiority of the CoCe-MA catalyst among the CoCe-X catalysts.

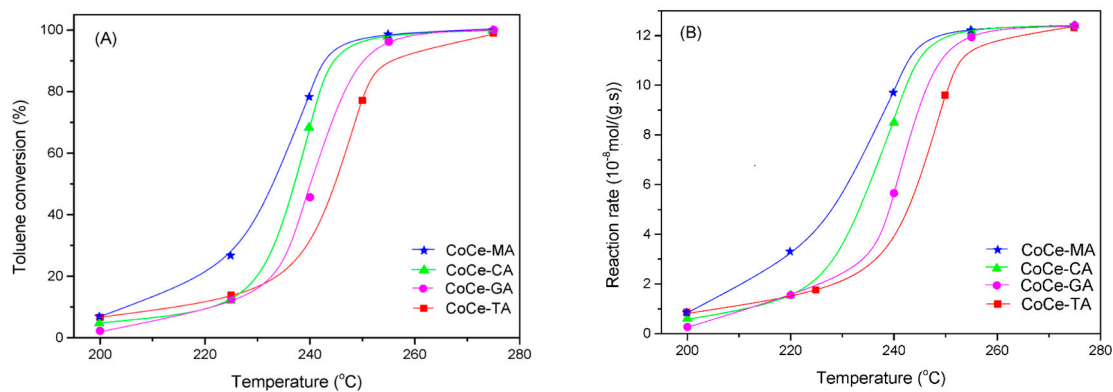


Figure 7. Toluene conversion (A); and reaction rate (B) as a function of reaction temperature over the CoCe-X catalysts. Reaction conditions: 500 ppm toluene, balanced dry air, total flow rate: 100 mL/min, 300 mg catalyst, GHSV = 20,000 mL/(g·h).

To evaluate the stability of the CoCe-X catalysts, the CoCe-MA catalyst was selected for the long-time test at 220 and 240 °C. The results are shown in Figure 8. During 48 h, the toluene conversion did not decrease significantly, indicating that the CoCe-MA catalyst had excellent catalytic stability.

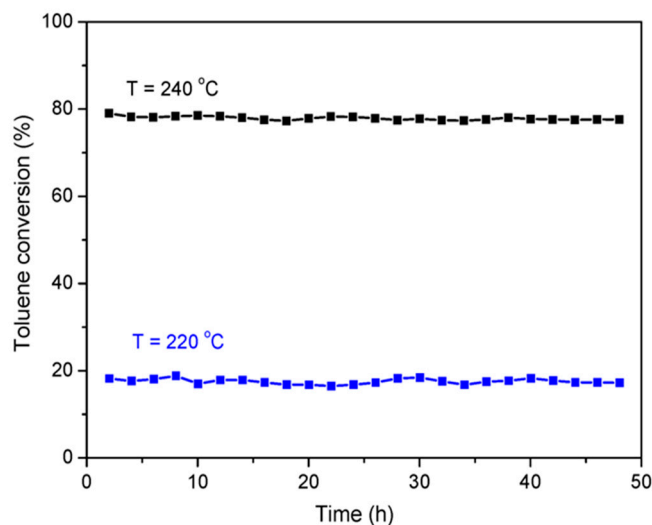


Figure 8. Long-time stability test for the CoCe-MA catalyst in the combustion of toluene at 220 and 240 °C. Reaction conditions: 500 ppm toluene, balanced dry air, total flow rate: 100 mL/min, 300 mg catalyst, GHSV = 20,000 mL/(g·h).

3. Discussion

In this study, cobalt cerium oxide catalysts were prepared via the sol-gel method, and four natural carboxylic acids were chosen as chelating agents in the preparation process. As is known, there are two main reactions involved in the sol-gel process: (1) hydrolysis of the precursors; and (2) condensation of the hydrolyzed products [46]. The nature of the chelating agents could influence the hydrolysis and condensation reactions, and then strongly affect the properties of the metal oxides synthesized. For example, the chosen organic acids possessed distinct acidity, molecular structures and thermal properties. The acidity of organic acids affected the hydrolysis reaction, while its molecular structure influenced the condensation process. As revealed by the TG-DSC curves, the weight loss and thermal released during the calcination strongly depended on the organic acids used. Therefore, not only the processes of hydrolysis and condensation but also calcination could be influenced by the nature of organic acids [31,47]. Furthermore, such variation in the preparation process could give rise to a series of differences in the textural and physicochemical properties of metal oxides synthesized. According to the characterization results, the type of organic acids affected neither the composition nor structure of the oxides obtained, while they did alter the crystallite size, textural property, and morphology of the catalysts. According to the H₂-TPR results, the CoCe-MA catalyst possessed the best reducibility, while the CoCe-TA was relatively the worst among these catalysts. Besides, it could be confirmed that, in the CoCe-MA and CoCe-CA catalysts, the cobalt species shared a homogeneous interaction with CeO₂ phase, which may enhance their catalytic performance. Consequently, the nature of the organic acids used as chelating agents has an important influence on the crystal size, morphology, and redox properties of the metal oxides obtained.

As for surface chemistry, the atomic ratio of O_{ads}/O_{lat} varies with the type of SOAs, and the maximum O_{ads}/O_{lat} value was obtained with the CoCe-MA catalyst. Figure 9 shows the relationship between the O_{ads}/O_{lat} and catalytic activity (T_{50} , T_{90}). As shown in this figure, the T_{50} and T_{90} gradually declined with the increase of O_{ads}/O_{lat}. As is known, the lower are the T_{50} and T_{90} values, the better is the catalytic activity. Thus, the order of catalytic activity was the same as that of surface O_{ads}/O_{lat} atomic ratios. As revealed by the literature [39,41], not only the surface oxygen species but also the distribution of the valence of the metal ions can affect the catalytic activity by the number of oxygen vacancies. The nonstoichiometric Co²⁺, as well as the presence of Ce³⁺ on the surface, could increase the vacancies and unsaturated chemical bonds on the surface, resulting in more surface oxygen species. The relationship between the T_{90} and surface Co²⁺/Co³⁺, Ce³⁺/Ce⁴⁺ atomic ratios is shown in Figure 10.

The results show that the surface $\text{Co}^{2+}/\text{Co}^{3+}$, $\text{Ce}^{3+}/\text{Ce}^{4+}$ atomic ratios decreased with increasing T_{90} values. In addition, the XPS spectra of the CoCe–MA–used catalyst is shown in Figure S1, and the quantitative estimates result is summarized in Table 6. As shown in Table 6, the surface atomic ratios of $O_{\text{ads}}/O_{\text{lat}}$, $\text{Co}^{2+}/\text{Co}^{3+}$ and $\text{Ce}^{3+}/\text{Ce}^{4+}$ of the CoCe–MA catalyst slightly decreased after the reaction, indicating that the active oxygen species at the surface took part in and played an important role in the oxidation reaction.

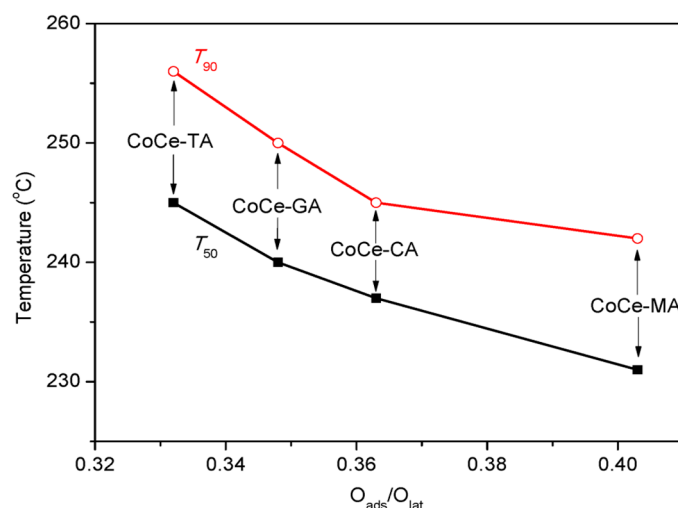


Figure 9. The relationship between surface $O_{\text{ads}}/O_{\text{lat}}$ ratio and catalytic activities (T_{50} , T_{90}).

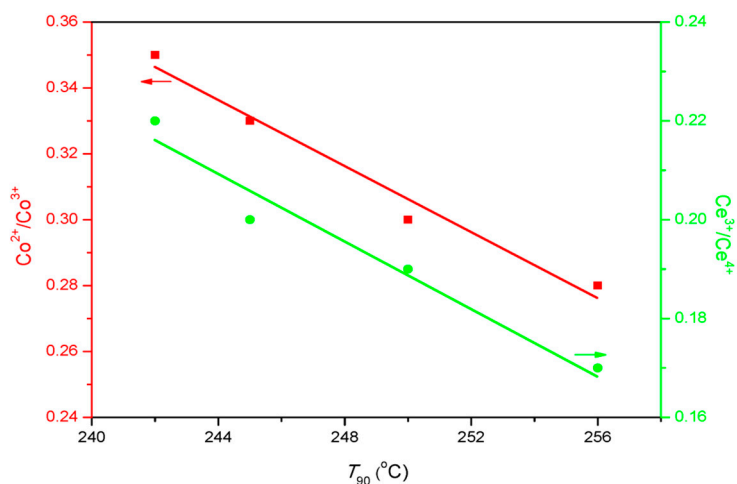


Figure 10. The relationship between T_{90} (90% toluene conversion temperatures) and surface $\text{Co}^{2+}/\text{Co}^{3+}$, $\text{Ce}^{3+}/\text{Ce}^{4+}$ ratios.

Table 6. Surface atomic ratios of the CoCe–MA catalyst before and after reaction.

Sample	Atomic Ratio		
	$O_{\text{ads}}/O_{\text{lat}}$	$\text{Co}^{2+}/\text{Co}^{3+}$	$\text{Ce}^{3+}/\text{Ce}^{4+}$
CoCe–MA	0.40	0.35	0.22
CoCe–MA–used	0.27	0.24	0.17

The types of organic acids caused the differences in the physicochemical properties of the CoCe–X catalysts and then led to the variation of the catalytic activity. As shown in Figure 7, the CoCe–MA catalyst exhibited the best catalytic performance. The catalytic activity of the CoCe–MA catalyst was extensively compared with other representative catalysts used for toluene oxidation in the literature [26,48–52], as displayed in Table 7. Table 7 shows that the T_{90} values of most catalysts in

toluene conversion were higher than that of the CoCe–MA catalyst. This indicated that the superiority of the CoCe–MA catalyst in the complete oxidation of toluene.

Table 7. Comparison of catalytic performance for toluene oxidation over typical metal oxides catalysts.

Catalyst	GHSV (mL/(g·h))	Concentration (ppm)	T_{90} (°C)	References
CoCe–MA	20,000	500	242	this work
CuMn _{0.5}	60,000	1200	273	[48]
CoMn _{0.5}	60,000	1200	258	[48]
Mn ₁ Co ₁	30,000	1000	249	[49]
CoAl ₅ –70	60,000	1000	298	[50]
CoAl ₃ –70	60,000	1000	281	[50]
Cu ₁ Mn ₁ O–600	20,000	1000	243	[51]
MOF ^a –Mn ₁ Co ₂	96,000	500	270	[52]
Cu ₁ Mn ₆	24,000	500	255	[26]
Cu ₁ Ce ₆	24,000	500	259	[26]

^a MOF: metal–organic frameworks.

In conclusion, the type of organic acids selected influenced the hydrolysis and condensation reactions, and then strongly affected the properties of the metal oxides synthesized. The CoCe–MA catalysts showed better catalytic performance than the CoCe–CA as well as other catalysts. The better catalytic performance of the CoCe–MA catalyst can be related to its texture, redox properties and unique surface compositions. Additionally, this paper provides an alternative for the choice of the chelating agent in the sol–gel method. Besides the commonly used citric acid, malic acid could also give excellent performance.

4. Materials and Methods

4.1. Catalyst Preparation

Cobalt cerium oxide catalysts were prepared by the sol–gel method. Firstly, a certain amount of Ce(NO₃)₃·6H₂O and Co(NO₃)₂·6H₂O (Shanghai, China) (Co/(Ce+Co) molar ratio was 0.70 [53]) were dissolved in deionized water, and then the selected organic acid was added into the solution under magnetic stirring for 30 min at 60 °C to form a homogeneous solution. The molar ratio of the organic acid to total metal ions was set as 1.2. After that, the mixture was evaporated in a rotary evaporator at 90 °C to produce viscous syrup which was then decomposed at 200 °C. Finally, the solids were ground and calcined at 550 °C in air for 4 h with a heating rate of 2 °C/min. The respective catalysts were marked as CoCe–X, where “X” represents MA, CA, GA, or TA.

4.2. Catalyst Characterization

The thermal decomposition behavior of CoCe–X precursors was evaluated by the thermal analyzer (NETZSCH–STA 409 PC, Beijing, China) with thermogravimetric analysis (TG) and differential scanning calorimetry (DSC). In the air atmosphere, the temperature rises from room temperature to 800 °C with the heating rate of 10 °C/min.

The crystallinity of the CoCe–X catalysts was tested by Rigaku D/MAX–2500PC X–ray diffractometer using Ni–filtered Cu K radiation. During the analysis, the CoCe–X catalysts were scanned from 10° to 70° with a speed of 5°/min. The crystallite sizes of the CoCe–X catalysts were estimated by Shelley equation.

The nitrogen adsorption–desorption isotherms were obtained at –196 °C on a Micromeritics ASAP 2010 system (Norcross, Georgia, USA). Prior to N₂ adsorption, the samples were degassed at 250 °C for 3 h. The Brunauer–Emmett–Teller (BET) equation was used to obtain the specific surface area of the CoCe–X catalysts. The Barrett–Joyner–Halenda (BJH) method was used to measure the pore volume and pore size distribution from the desorption branches of isotherms.

The surface morphology and element content of the CoCe–X catalysts were measured by scanning electron microscopy (SEM, Hitachi S–4700, Tokyo, Japan) and energy dispersive X–ray spectroscopy (EDS) data. The CoCe–X catalysts were firstly coated on double–sided tape and then platinum sprayed. The images of CoCe–X catalysts at different magnification were obtained, and their element contents were measured by EDS.

The CoCe–X catalysts were analyzed by X–ray photoelectron spectroscopy (XPS) with Thermo–Fisher Escalab 250xi electron spectrometer (Waltham, MA, USA) using Al Ka (1486.6 eV) radiation source. In this characterization, the C 1s core level induced by carbon in the catalyst was selected as a reference, and its binding energy was fixed at 284.8 eV. The XPS curves of the CoCe–X catalysts were fitted by XPSPEAK41 software.

The hydrogen temperature programmed reduction (H₂–TPR) analysis over CoCe–X catalysts were carried out on 2910 microcirculation chemisorption analyzer equipped with thermal conductivity detector (TCD). Before the testing, the CoCe–X catalysts were pretreated at 450 °C for 1 h with 5% O₂/He flow rate (50 mL/min), and then cooled to 50 °C in the same gas stream. Then, the reducing gas was introduced at the flow rate of 50 mL/min (10 vol.% H₂/N₂), and the reactor was heated from 50 to 900 °C with a rate of 10 °C/min. The response of TCD was calibrated with Micromeritics silver oxide.

4.3. Catalyst Evaluation

The catalytic performance of the CoCe–X catalysts was tested in a fixed bed quartz reactor (8 mm i.d.). The typical reaction conditions were as follows: 300 mg (40–60 mesh) samples, 500 ppm toluene, balanced dry air, total flow rate of 100 mL/min, and the gas hourly space velocity (GHSV) of 20,000 mL/(g·h). Before each test, to avoid overestimation of toluene conversion (caused by adsorption), the reactor was maintained 2 h at 100 °C. The concentration of toluene in the outlet of 100 °C was taken as the initial inlet concentration. The gas chromatograph (GC1620, Shimadzu, Shaghai, China.) equipped with a flame ionization detector (FID) was used to determine the concentration of toluene in the outlet gas. The average values of three steady–state measurements at each temperature were marked as the final data at that temperature.

5. Conclusions

Cobalt cerium oxide catalysts were prepared via the sol–gel method, and four natural carboxylic acids were chosen as chelating agents in the preparation process. Their catalytic performance towards toluene combustion was evaluated. If T_{90} was used as the activity standard, the order of activity of the CoCe–X catalysts was as follows: CoCe–MA > CoCe–CA > CoCe–GA > CoCe–TA. The CoCe–MA catalyst showed the highest catalytic activity, which reached 90% of the toluene conversion rate at 242 °C. Moreover, the effects of small–molecule organic acids as chelating agents on the composition, structure, and morphology of the CoCe–X catalysts synthesized are discussed in detail. The results of SEM, XRD, and N₂–adsorption and desorption measurements show that the type of organic acids affected neither the composition nor structure of the oxides obtained, while they did alter the crystallite size, textual property, and morphology of the catalysts. XPS results suggest that the type of SOAs has an important influence on the distribution of surface oxygen species and oxidation states of the metal ions. The order of catalytic activity was the same as that of surface O_{ads}/O_{lat} atomic ratio. In addition, the surface oxidation state of Co²⁺/Co³⁺ and Ce³⁺/Ce⁴⁺ played an important role in the catalytic performance of the cobalt cerium oxides catalysts. TPR results reveal that the CoCe–MA catalyst possessed the best reducibility, and, in the CoCe–MA and CoCe–CA catalysts, the cobalt species shared a homogeneous interaction with CeO₂ phase, which enhanced their catalytic performance. Thus, compared with the other three samples, the better catalytic performance of CoCe–MA catalyst could be related to its textural, redox properties and unique surface compositions and oxidation states.

Supplementary Materials: The following are available online at <http://www.mdpi.com/2073-4344/9/5/483/s1>, Figure S1: Experimental and fitted (A) O 1s, (B) Co 2p and (C) Ce 3d photoelectron spectra of the CoCe-MA-used catalyst.

Author Contributions: Conceptualization, J.L., J.W., J.C. (Jianmeng Chen) and J.C. (Jinghuan Chen); methodology, J.L., J.W., J.C. (Jianmeng Chen) and J.C. (Jinghuan Chen); validation, J.L.; formal analysis, J.L. and J.C. (Jinghuan Chen); investigation, J.L.; resources, J.W.; data curation, J.L. and J.C. (Jinghuan Chen); writing—original draft preparation, J.L.; writing—review and editing, J.C. (Jianmeng Chen) and J.C. (Jinghuan Chen); supervision, J.C. (Jinghuan Chen); and funding acquisition, J.C. (Jianmeng Chen).

Funding: This work was supported by the National key R&D Program of China (Grant No. 2018YFC0214100) and the National Natural Science Foundation of China (Grant No. 51406179).

Conflicts of Interest: The authors declare no conflict of interest.

References

1. Li, Y.; Fan, Z.; Shi, J.; Liu, Z.; Zhou, J.; Shangguan, W. Removal of volatile organic compounds (VOCs) at room temperature using dielectric Bbarrier discharge and plasma-catalysis. *Plasma Chem. Plasma P.* **2014**, *34*, 801–810. [[CrossRef](#)]
2. Zuo, S.F.; Huang, Q.Q.; Li, J.; Zhou, R.X. Promoting effect of Ce added to metal oxide supported on Al pillared clays for deep benzene oxidation. *Appl. Catal. B Environ.* **2009**, *91*, 204–209. [[CrossRef](#)]
3. Huang, H.; Xu, Y.; Feng, Q.; Leung, D.Y.C. Low temperature catalytic oxidation of volatile organic compounds: a review. *Catal. Sci. Technol.* **2015**, *5*, 2649–2669. [[CrossRef](#)]
4. Zhang, Z.; Jiang, Z.; Shangguan, W. Low-temperature catalysis for VOCs removal in technology and application: A state-of-the-art review. *Catal. Today* **2016**, *264*, 270–278. [[CrossRef](#)]
5. Kim, S.C.; Nahm, S.W.; Shim, W.G.; Lee, J.W.; Moon, H. Influence of physicochemical treatments on spent palladium based catalyst for catalytic oxidation of VOCs. *J. Hazard. Mater.* **2007**, *141*, 305–314. [[CrossRef](#)]
6. Bonelli, R.; Lucarelli, C.; Pasini, T.; Liotta, L.F.; Zacchini, S.; Albonetti, S. Total oxidation of volatile organic compounds on Au/FeO_x catalysts supported on mesoporous SBA-15 silica. *Appl. Catal. A Gen.* **2011**, *400*, 54–60. [[CrossRef](#)]
7. Chen, H.; Zhang, H.; Yan, Y. Fabrication of porous copper/manganese binary oxides modified ZSM-5 membrane catalyst and potential application in the removal of VOCs. *Chem. Eng. J.* **2014**, *254*, 133–142. [[CrossRef](#)]
8. Liao, Y.; Zhang, X.; Peng, R.; Zhao, M.; Ye, D. Catalytic properties of manganese oxide polyhedra with hollow and solid morphologies in toluene removal. *Appl. Surf. Sci.* **2017**, *405*, 20–28. [[CrossRef](#)]
9. Carabineiro, S.A.C.; Chen, X.; Konsolakis, M.; Psarras, A.C.; Tavares, P.B.; Orfao, J.J.M.; Pereira, M.F.R.; Figueiredo, J.L. Catalytic oxidation of toluene on Ce-Co and La-Co mixed oxides synthesized by exotemplating and evaporation methods. *Catal. Today* **2015**, *244*, 161–171. [[CrossRef](#)]
10. Barakat, T.; Rooke, J.C.; Tidahy, H.L.; Hosseini, M.; Cousin, R.; Lamonier, J.F.; Giraudon, J.M.; De Weireld, G.; Su, B.L.; Siffert, S. Noble-metal-based catalysts supported on zeolites and macro-mesoporous metal oxide supports for the total oxidation of volatile organic compounds. *ChemSusChem* **2011**, *4*, 1420–1430. [[CrossRef](#)]
11. Chen, J.; Shi, W.; Zhang, X.; Arandiyani, H.; Li, D.; Li, J. Roles of Li⁺ and Zr⁴⁺ cations in the catalytic performances of Co_{1-x}M_xCr₂O₄ (M = Li, Zr; x=0–0.2) for methane combustion. *Environ. Sci. Technol.* **2011**, *45*, 8491–8497. [[CrossRef](#)]
12. Li, W.B.; Wang, J.X.; Gong, H. Catalytic combustion of VOCs on non-noble metal catalysts. *Catal. Today* **2009**, *148*, 81–87. [[CrossRef](#)]
13. Tang, W.; Liu, G.; Li, D.; Liu, H.; Wu, X.; Han, N.; Chen, Y. Design and synthesis of porous non-noble metal oxides for catalytic removal of VOCs. *Sci. China Chem.* **2015**, *58*, 1359–1366. [[CrossRef](#)]
14. Zabihi, M.; Khorasheh, F.; Shayegan, J. Supported copper and cobalt oxides on activated carbon for simultaneous oxidation of toluene and cyclohexane in air. *RSC Adv.* **2015**, *5*, 5107–5122. [[CrossRef](#)]
15. Liu, Y.; Deng, J.; Xie, S.; Wang, Z.; Dai, H. Catalytic removal of volatile organic compounds using ordered porous transition metal oxide and supported noble metal catalysts. *Chin. J. Catal.* **2016**, *37*, 1193–1205. [[CrossRef](#)]
16. Feng, X.; Guo, J.; Wen, X.; Xu, M.; Chu, Y.; Yuan, S. Enhancing performance of Co/CeO₂ catalyst by Sr doping for catalytic combustion of toluene. *Appl. Surf. Sci.* **2018**, *445*.
17. Yan, C.F.; Chen, H.; Hu, R.R.; Huang, S.; Luo, W.; Guo, C.; Li, M.; Li, W. Synthesis of mesoporous Co-Ce oxides catalysts by glycine-nitrate combustion approach for CO preferential oxidation reaction in excess H₂. *Int. J. Hydrogen Energy* **2014**, *39*, 18695–18701. [[CrossRef](#)]

18. Dai, Q.; Wang, X.; Lu, G. Low-temperature catalytic combustion of trichloroethylene over cerium oxide and catalyst deactivation. *Appl. Catal. B Environ.* **2008**, *81*, 192–202. [[CrossRef](#)]
19. Liotta, L.F.; Di Carlo, G.; Pantaleo, G.; Venezia, A.M.; Deganello, G. $\text{Co}_3\text{O}_4/\text{CeO}_2$ composite oxides for methane emissions abatement: relationship between $\text{Co}_3\text{O}_4\text{-CeO}_2$ interaction and catalytic activity. *Appl. Catal. B Environ.* **2006**, *66*, 217–227. [[CrossRef](#)]
20. Konsolakis, M.; Sgourakis, M.; Carabineiro, S.A.C. Surface and redox properties of cobalt–ceria binary oxides: on the effect of Co content and pretreatment conditions. *Appl. Surf. Sci.* **2015**, *341*, 48–54. [[CrossRef](#)]
21. Li, H.; Lu, G.; Qiao, D.; Wang, Y.; Guo, Y.; Guo, Y. Catalytic methane combustion over $\text{Co}_3\text{O}_4/\text{CeO}_2$ composite oxides prepared by modified citrate sol–gel method. *Catal. Lett.* **2011**, *141*, 452–458. [[CrossRef](#)]
22. Liotta, L.F.; Ousmane, M.; Di Carlo, G.; Pantaleo, G.; Deganello, G.; Marci, G.; Retailleau, L.; Giroir-Fendler, A. Total oxidation of propene at low temperature over $\text{Co}_3\text{O}_4\text{-CeO}_2$ mixed oxides: role of surface oxygen vacancies and bulk oxygen mobility in the catalytic activity. *Applied Catalysis A Gen.* **2008**, *347*, 81–88. [[CrossRef](#)]
23. Mei, J.; Ke, Y.; Yu, Z.; Hu, X.; Qu, Z.; Yan, N. Morphology–dependent properties of $\text{Co}_3\text{O}_4/\text{CeO}_2$ catalysts for low temperature dibromomethane (CH_2Br_2) oxidation. *Chem. Eng. J.* **2017**, *320*, 124–134. [[CrossRef](#)]
24. Deng, W.; Dai, Q.; Lao, Y.; Shi, B.; Wang, X. Low temperature catalytic combustion of 1,2-dichlorobenzene over $\text{CeO}_2\text{-TiO}_2$ mixed oxide catalysts. *Appl. Catal. B Environ.* **2016**, *181*, 848–861. [[CrossRef](#)]
25. Zhang, X.; Pei, Z.; Wu, T.; Lu, H.; Huang, H. A mechanistic study of the sulfur tolerance of Cu–V mixed oxides in toluene catalytic combustion. *React. Kinet. Mech. Catal.* **2015**, *116*, 467–478. [[CrossRef](#)]
26. Lu, H.; Kong, X.; Huang, H.; Zhou, Y.; Chen, Y. Cu–Mn–Ce ternary mixed–oxide catalysts for catalytic combustion of toluene. *J. Environ. Sci.* **2015**, *32*, 102–107. [[CrossRef](#)]
27. Liu, C.; Luo, L.; Lu, X. Preparation of mesoporous $\text{Ce}_{1-x}\text{Fe}_x\text{O}_2$ mixed oxides and their catalytic properties in methane combustion. *Kinet. Catal.* **2008**, *49*, 676–681. [[CrossRef](#)]
28. Gao, L.; Li, C.; Zhang, J.; Du, X.; Li, S.; Zeng, J.; Yi, Y.; Zeng, G. Simultaneous removal of NO and Hg^0 from simulated flue gas over $\text{CoO}_x\text{-CeO}_2$ loaded biomass activated carbon derived from maize straw at low temperatures. *Chem. Eng. J.* **2018**, 342.
29. Sanpo, N.; Wang, J.; Ang, A.S.M.; Berndt, C.C. Influence of the different organic chelating agents on the topography, physical properties and phase of SPPS–deposited spinel ferrite splats. *Appl. Surf. Sci.* **2013**, *284*, 171–178. [[CrossRef](#)]
30. Wang, D.; Cao, L.; Huang, J.; Wu, J. Effects of different chelating agents on the composition, morphology and electrochemical properties of LiV_3O_8 crystallites synthesized via sol–gel method. *Ceram. Int.* **2013**, *39*, 3759–3764. [[CrossRef](#)]
31. Hessian, M.M.; Mostafa, N.Y.; Abd-Elkader, O.H. Influence of carboxylic acid type on microstructure and magnetic properties of polymeric complex sol–gel driven NiFe_2O_4 . *J. Magn. Magn. Mater.* **2016**, *398*, 109–115. [[CrossRef](#)]
32. Li, W.; Lee, J. Microwave–assisted sol–gel synthesis and photoluminescence characterization of $\text{LaPO}_4: \text{Eu}^{3+}, \text{Li}^+$ nanophosphors. *J. Phys. Chem. C* **2008**, *112*, 11679–11684. [[CrossRef](#)]
33. Vinaykumar, R.; Mazumder, R.; Bera, J. Characterization of $\text{SrCo}_{0.5}\text{Ti}_{1.5}\text{Fe}_9\text{O}_{19}$ hexagonal ferrite synthesized by solgel combustion and solid state route. *J. Magn. Magn. Mater.* **2017**, *429*, 359–366. [[CrossRef](#)]
34. Luo, J.Y.; Meng, M.; Li, X.; Li, X.G.; Zha, Y.Q.; Hu, T.D.; Xie, Y.N.; Zhang, J. Mesoporous $\text{Co}_3\text{O}_4\text{-CeO}_2$ and $\text{Pd}/\text{Co}_3\text{O}_4\text{-CeO}_2$ catalysts: Synthesis, characterization and mechanistic study of their catalytic properties for low–temperature CO oxidation. *J. Catal.* **2008**, *254*, 310–324. [[CrossRef](#)]
35. Chen, J.; Cao, F.; Qu, R.; Gao, X.; Cen, K. Bimetallic cerium–copper nanoparticles embedded in ordered mesoporous carbons as effective catalysts for the selective catalytic reduction of NO with NH_3 . *J. Colloid Interface Sci.* **2015**, *456*, 66–75. [[CrossRef](#)] [[PubMed](#)]
36. Li, J.; Fu, H.; Fu, L.; Hao, J. Complete combustion of methane over indium tin oxides catalysts. *Environ. Sci. Technol.* **2006**, *40*, 6455–6459. [[CrossRef](#)]
37. Cai, T.; Huang, H.; Deng, W.; Dai, Q.; Liu, W.; Wang, X. Catalytic combustion of 1,2-dichlorobenzene at low temperature over Mn–modified Co_3O_4 catalysts. *Appl. Catal. B Environ.* **2015**, *166*, 393–405. [[CrossRef](#)]
38. Solsona, B.; Davies, T.E.; Garcia, T.; Vazquez, I.; Dejoz, A.; Taylor, S.H. Total oxidation of propane using nanocrystalline cobalt oxide and supported cobalt oxide catalysts. *Appl. Catal. B Environ.* **2008**, *84*, 176–184. [[CrossRef](#)]

39. Gonzalez-Prior, J.; Lopez-Fonseca, R.; Gutierrez-Ortiz, J.I.; de Rivas, B. Catalytic removal of chlorinated compounds over ordered mesoporous cobalt oxides synthesised by hard-templating. *Appl. Catal. B Environ.* **2018**, *222*, 9–17.
40. Zhao, L.; Li, C.; Li, S.; Wang, Y.; Zhang, J.; Wang, T.; Zeng, G. Simultaneous removal of elemental mercury and NO in simulated flue gas over V₂O₅/ZrO₂-CeO₂ catalyst. *Appl. Catal. B Environ.* **2016**, *198*, 420–430. [[CrossRef](#)]
41. Chen, J.; Li, C.; Li, S.; Lu, P.; Gao, L.; Du, X.; Yi, Y. Simultaneous removal of HCHO and elemental mercury from flue gas over Co-Ce oxides supported on activated coke impregnated by sulfuric acid. *Chem. Eng. J.* **2018**, *338*, 358–368. [[CrossRef](#)]
42. Russo, N.; Furfori, S.; Fino, D.; Saracco, G.; Specchia, V. Lanthanum cobaltite catalysts for diesel soot combustion. *Appl. Catal. B Environ.* **2008**, *83*, 85–95. [[CrossRef](#)]
43. Liotta, L.F.; Di Carlo, G.; Pantaleo, G.; Deganello, G. Co₃O₄/CeO₂ and Co₃O₄/CeO₂-ZrO₂ composite catalysts for methane combustion: Correlation between morphology reduction properties and catalytic activity. *Catal. Commun.* **2005**, *6*, 329–336. [[CrossRef](#)]
44. Konsolakis, M.; Ioakeimidis, Z. Surface/structure functionalization of copper-based catalysts by metal-support and/or metal-metal interactions. *Appl. Surf. Sci.* **2014**, *320*, 244–255. [[CrossRef](#)]
45. Cheng, H.; Yuan, W.; Scott, K.; Browning, D.J.; Lakeman, J.B. The catalytic activity and methanol tolerance of transition metal modified-ruthenium-selenium catalysts. *Appl. Catal. B Environ.* **2007**, *75*, 221–228. [[CrossRef](#)]
46. Baccile, N.; Babonneau, F.; Thomas, B.; Coradin, T. Introducing ecodesign in silica sol-gel materials. *J. Mater. Chem.* **2009**, *19*, 8537–8559. [[CrossRef](#)]
47. Danks, A.E.; Hall, S.R.; Schnepf, Z. The evolution of ‘sol-gel’ chemistry as a technique for materials synthesis. *Mater. Horiz.* **2016**, *3*, 91–112. [[CrossRef](#)]
48. Antonio Aguilera, D.; Perez, A.; Molina, R.; Moreno, S. Cu-Mn and Co-Mn catalysts synthesized from hydrotalcites and their use in the oxidation of VOCs. *Appl. Catal. B Environ.* **2011**, *104*, 144–150. [[CrossRef](#)]
49. Qu, Z.; Gao, K.; Fu, Q.; Qin, Y. Low-temperature catalytic oxidation of toluene over nanocrystal-like Mn-Co oxides prepared by two-step hydrothermal method. *Catal. Commun.* **2014**, *52*, 31–35. [[CrossRef](#)]
50. Bialas, A.; Mazur, M.; Natkanski, P.; Dudek, B.; Kozak, M.; Wach, A.; Kustrowski, P. Hydrotalcite-derived cobalt-aluminum mixed oxide catalysts for toluene combustion. *Appl. Surf. Sci.* **2016**, *362*, 297–303. [[CrossRef](#)]
51. Hu, J.; Li, W.B.; Liu, R.F. Highly efficient copper-doped manganese oxide nanorod catalysts derived from CuMnO hierarchical nanowire for catalytic combustion of VOCs. *Catal. Today* **2018**, *314*, 147–153. [[CrossRef](#)]
52. Luo, Y.; Zheng, Y.; Zuo, J.; Feng, X.; Wang, X.; Zhang, T.; Zhang, K.; Jiang, L. Insights into the high performance of Mn-Co oxides derived from metal organic frameworks for total toluene oxidation. *J. Hazard. Mater.* **2018**, *349*, 119–127. [[CrossRef](#)] [[PubMed](#)]
53. Wang, C.; Zhang, C.; Hua, W.; Guo, Y.; Lu, G.; Gil, S.; Giroir-Fendler, A. Catalytic oxidation of vinyl chloride emissions over Co-Ce composite oxide catalysts. *Chem. Eng. J.* **2017**, *315*, 392–402. [[CrossRef](#)]

